Design of Misalignment-Insensitive Inductive Power Transfer via Interoperable Coil Module and Dynamic Power Control

Tsong-Shing Lee, Shyh-Jier Huang, *Senior Member, IEEE*, Shuo-Huei Dai, and Jun-Li Su

***Abstract*—This article proposes a misalignment-insensitive inductive power transfer (IPT) via interoperable tricoil module and dynamic power control. Since the misaligned coils is known to affect the power transmission efficiency and coupling performance, the article is devoted to the design of an interoperable tricoil module along with power modulation technique in the anticipation of reaching the misalignment-insensitive IPT. In this circuit design, three half-bridge inverters are deployed to drive three transmitting coils. Both geometric structure and magnetic field of coil modules are assessed. A dynamic power control strategy is implemented to adjust the amount of transferable power following the determination of the direction of movement of receiving coils, ensuring a higher efficiency of power transfer and coupling balance at the time of misalignment. To validate the practicality of this approach, the hardware prototype of tricoil module with IPT capability of 3.2-kW is realized with a 7% improvement of efficiency at a misalignment of 100 mm. These results support the feasibility of the proposed approach, serving as beneficial references for automatic guided vehicle applications.**

***Index Terms*—Inductive power transfer (IPT), misalignment, tricoil module.**

I. Introduction

SEVERAL countries are constantly endeavored to develop transportation electrification, electrically powered vehicles, and automated guided vehicle (AGV), yet the way of plugging power often encountered the problems of aging connectors and rusted components during the charging process [1]–[3]. The inductive power transfer (IPT) hence emerged as a practical alternative for transportation and electrification applications [4]–[8]. Yet, from the perspective of practitioners, the efficiency of wireless power transmission was easily affected once coils were not aligned. This also implies that more efforts are required to increase the misalignment tolerance and balance the magnetic coupling, which meanwhile motivates the study made in this article.

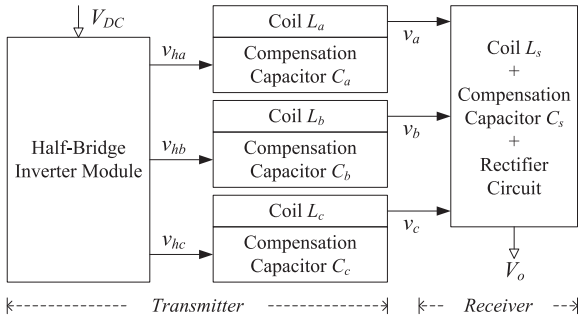

Fig. 1. Block diagram of the interoperable IPT system.

Previous charging-related studies include one-to-one charging [9]–[12], one-to-many charging [13]–[17], and many-to-one charging [18]–[24]. Based on these published techniques, the magnetic field distribution at the transmitting side of one-to-one charging system was found to decay from the center to the outward coil. Particularly, for those misaligned coils, their magnetic fields were significantly reduced, resulting in the degradation of charging performance [9]–[12]. In view of this degraded performance, the utilization of multiple receiving coils was suggested, where each device receives the power individually [13]–[17]. This method was reported feasible, yet the uneven distribution of magnetic fields caused different reflected impedances and brought the difficulty in maintaining a constant supplying power. Subsequently, a many-to-one contactless power supply was proposed, where multi-transmitting coils and a receiving coil were both included [23]–[25]. Although the magnetic field became more evenly distributed, yet the system lacked the investigation of coil geometry and coupling characteristics under the situation of misalignment.

Different from previous literatures, this article presents an interoperable tricoil module to reach the misalignment-insensitive IPT. Fig. 1 is the block diagram of the proposed system, where a feedback control loop assists in the dynamic power control of each coil during the period of charging. The symmetrical radial placement is made based on the analysis of coil geometry, coupling gain, and magnetic field. A compensation circuit is also

Manuscript received August 15, 2019; revised November 2, 2019 and December 30, 2019; accepted January 29, 2020. Date of publication February 6, 2020; date of current version May 1, 2020. Recommended for publication by Associate Editor M. Ponce-Silva. *(Corresponding author: Shyh-Jier Huang.)*

Tsong-Shing Lee is with the Department of Electrical Engineering, Southern Taiwan University of Science and Technology, Tainan 71005, Taiwan (e-mail: tslee@stust.edu.tw).

Shyh-Jier Huang is with the Department of Electrical Engineering, National Cheng Kung University, Tainan 70101, Taiwan (e-mail: clhuang@mail.ncku.edu.tw).

Shuo-Huei Dai is with the Himax Technologies, Inc., Tainan 74148, Taiwan (e-mail: s910173@gmail.com).

Jun-Li Su is with the Delta Electronics, Inc., Tainan 74144, Taiwan (e-mail: infinite1827@gmail.com).

Color versions of one or more of the figures in this article are available online at https://ieeexplore.ieee.org.

Digital Object Identifier 10.1109/TPEL.2020.2972035

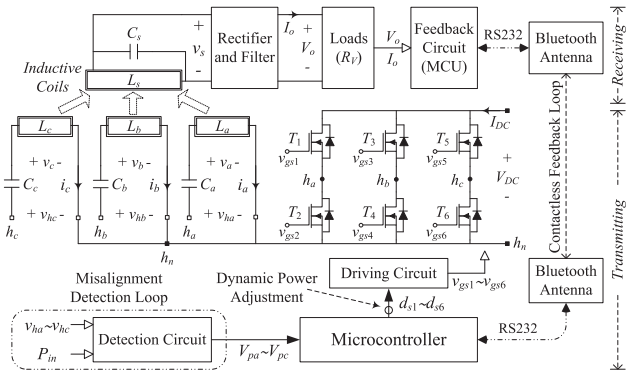

Fig. 2. Configuration of the proposed system.

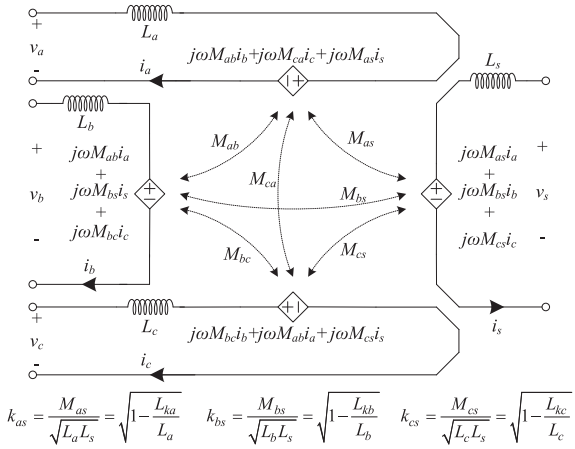

Fig. 3. Equivalent model of coil transmitting structure.

designed to maintain the coupling balance and uniform current distribution to cope with misalignment. Features of this proposed circuit are listed below.

1) The proposed design increases magnetic couplings via a tricoil module with radial symmetry placement, reaching a higher efficiency of power transfer when the receiving coil is not in good alignment with the transmitting one.
2) The circuit adds a detection method of misalignment as well as a dynamic power control mechanism in order to grasp the direction of coil movement. The approach excels at the adjustment of duty cycle of each switch in a more flexible manner.
3) The coil design along with coupling characteristics and voltage gain are systematically analyzed. This systematic approach is beneficial for the mass production of industry manufacturing, serving as useful references for guided vehicle and transportation charging applications.

The rest of this article is organized as follows. Section II introduces the proposed system, Section III investigates and realizes the interoperable coil module, Section IV describes the misalignment detection and dynamic power control strategies, Section V discusses the experimental results, and Section VI draws the conclusion.

II. Proposed System

A. Circuit Configuration

Fig. 2 delineates the circuit configuration of proposed system, where both transmitting side and receiving side are included. The transmitting side is composed of three half-bridge inverter modules, three inductive coil modules (L_a, L_b, and L_c), and three resonance compensation modules (C_a, C_b, and C_c). The receiving side contains an inductive coil (L_s), a compensation capacitor (C_s), and a full-wave rectifier circuit. In this system, an input dc voltage $V_{\rm dc}$ of 415.6 V from the power-factor-correction (PFC) circuit is used. The power transfer process involves using half-bridge inverters along with three inductive coils as well as asymmetric pulse-width-modulation control. The system starts with the conversion of input voltage $V_{\rm dc}$ to high-frequency alternating signals of v_a–v_c, by which magnetic fields are established via coils, inducing the secondary voltage of v_s so as to deliver power to rectifier and filter circuits for the subsequent charging.

In this system, the dynamic power control circuit is meanwhile implemented with the microcontroller to detect spike signals of rising edge of voltage v_{ha}, v_{hb}, and v_{hc} such that the transmitting power of each half-bridge inverter can be controlled. In the control circuit, two sets of microcontroller units (TMS320F28335, Texas Instruments Inc.) are embedded for power adjustment and contactless feedback. The antennas are employed for the contactless feedback such that silicon carbide n-channel MOSFETs T_1–T_6 (SCT2080KE, Rohm) are driven by signals of v_{gs1}–v_{gs6}. Note that the use of silicon carbide planar MOSFET is to take advantage of its high-voltage resistance, fast switching, large voltage rating, and low ON-resistance. A gate-driven photo-coupler isolation circuit is then adopted to convert the driving signals of d_{s1}–d_{s6} of 5 V to v_{gs1}–v_{gs6} of 15 V.

In this control loop, a detection circuit detects voltages of v_{ha}, v_{hb}, and v_{hc} as well as input voltage $V_{\rm dc}$ and input current $I_{\rm dc}$, while a feedback circuit grasps voltage V_o and current I_o at the load side. Through this work of detection and feedback, the output voltage is stabilized with the comprehension of coil-moving directions, hence assisting in adjusting duty cycles of inverters (v_{ha}, v_{hb}, and v_{hc}). The system works at an air gap of 200 mm under an operating frequency of 86 kHz. The coil geometry, coupling characteristics, dynamic power adjustment scheme, and resonance compensation are all investigated in the next section.

B. Resonance Gain Analysis of Interoperable Coil Module

Fig. 3 shows the equivalent model of the proposed coil structure. In the figure, L_a–L_c and L_s represent the self-inductance at transmitting side and receiving side, respectively. The mutual inductances between coils at the transmitting side are M_{ab}, M_{bc}, and M_{ca}, and the mutual inductances between each transmitting coil and receiving coil are M_{as}, M_{bs}, and M_{cs}. Meanwhile, the figure lists the coupling coefficient k_{as}, k_{bs}, and k_{cs} to express the relation between coupling coefficient and mutual inductance for each transmitting and receiving coils, where L_{ka}, L_{kb}, and L_{kc} individually represent the measured leakage inductance of coils L_a,L_b, and L_c, respectively. Considering that the compensation capacitances of series–parallel topology are

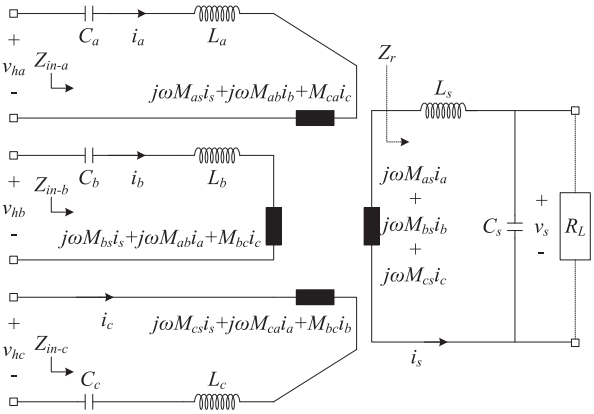

Fig. 4. Equivalent circuit model including compensation elements.

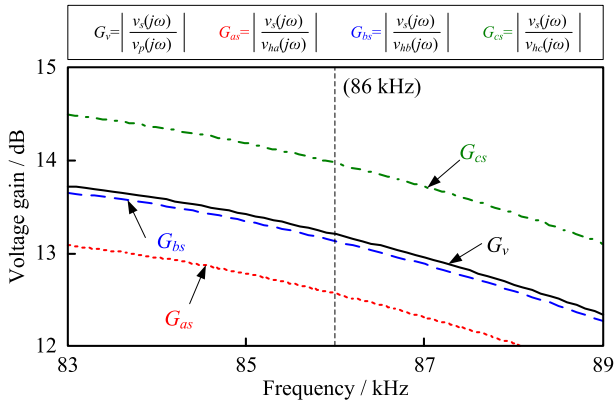

Fig. 5. Voltage gain as a function of frequency when the receiving coil is symmetrically aligned.

less affected by load variations [26], [27], this article chooses the series–parallel compensation circuit as depicted in Fig. 4, ensuring a more stable output voltage [28], [29].

In the plot of Fig. 4, $Z_{\text{in}-a}$, $Z_{\text{in}-b}$, and $Z_{\text{in}-c}$ are input impedances of each transmitting coil, and R_L is the equivalent load of full-wave rectifier circuit and charging network circuit at back stage. The compensation capacitance at the receiving side is derived based on the resonance frequency ω_0 as

$$C_s = 1/\omega_o^2 L_s. \tag{1}$$

The voltage–current relation at each transmitting and receiving side is individually expressed as

$$v_{\boldsymbol{ha}} = \left(\frac{1-\omega^2 C_a L_a}{j\omega C_a}\right)\boldsymbol{i_a} + j\omega(M_{as}\boldsymbol{i_s} + M_{ab}\boldsymbol{i_b} + M_{ca}\boldsymbol{i_c}) \tag{2}$$

$$\boldsymbol{v_{hb}} = \left(\frac{1-\omega^2 C_b L_b}{j\omega C_b}\right)\boldsymbol{i_b} + j\omega(M_{bs}\boldsymbol{i_s} + M_{ab}\boldsymbol{i_a} + M_{bc}\boldsymbol{i_c}) \tag{3}$$

$$\boldsymbol{v_{hc}} = \left(\frac{1-\omega^2 C_c L_c}{j\omega C_c}\right)\boldsymbol{i_c} + j\omega(M_{cs}\boldsymbol{i_s} + M_{ca}\boldsymbol{i_a} + M_{bc}\boldsymbol{i_b}) \tag{4}$$

$$\boldsymbol{v_s} = j\omega(M_{as}\boldsymbol{i_a} + M_{bs}\boldsymbol{i_b} + M_{cs}\boldsymbol{i_c}) + j\omega L_s \boldsymbol{i_s}. \tag{5}$$

By assuming the mutual inductances between coils at the transmitting side are approximately M_{tt} and the mutual inductances between each transmitting-coil and receiving-coil are approximately M_{tr}, the input impedance Z_{in} at the transmitting side can be derived as follows:

$$Z_{\text{in}}(\omega=\omega_o) = \frac{1-\omega_o^2 C_p(L_p+2M_{tt})}{j\omega_o C_p} + \frac{3\omega_o^2 M_{tr}^2 + 3j\omega_o^3 M_{tr}^2 C_s R_L}{j\omega_o L_s - \omega_o^2 L_s C_s R_L + R_L}. \tag{6}$$

Then, the parameter of C_p is calculated when $\omega = \omega_0$ by assuming the imaginary part of (8) amounting to zero [28], which

TABLE I
PARAMETERS OF THE PROPOSED SYSTEM

Symbol	Parameters	Values
L_a	Transmitting coil inductance	65.64 μH
L_b	Transmitting coil inductance	67.42 μH
L_c	Transmitting coil inductance	66.34 μH
L_s	Receiving coil inductance	44.76 μH
C_a	Transmitting compensated capacitance	64.62 nF
C_b	Transmitting compensated capacitance	66.48 nF
C_c	Transmitting compensated capacitance	65.62 nF
C_s	Receiving compensated capacitance	73.5 nF
M_{tr}	Mutual inductance between each transmitting coil and the receiving coil	8.336 μH
M_{tt}	Mutual inductance between every two transmitting coils	5.755 μH
k_{tr}	Coupling coefficient between each transmitting coil and the receiving coil	0.153
k_{tt}	Coupling coefficient between every two transmitting coils	0.113

is expressed as

$$C_p(\omega=\omega_o) = \frac{1}{\omega_o^2\left(L_p - \frac{3M_{tr}^2}{L_s} + 2M_{tt}\right)}. \tag{7}$$

The voltage gain $G_v(j\omega)$ of this resonance circuit from v_p to v_s becomes

$$G_v(j\omega) = \left|\frac{v_s(j\omega)}{v_p(j\omega)}\right| = \left|\frac{3j\omega M_{tr}}{Z_{in}(j\omega)} \times \frac{\frac{R_L}{1+j\omega C_s R_L}}{j\omega L_s + \frac{R_L}{1+j\omega C_s R_L}}\right|. \tag{8}$$

It is worth noting that through the adjustment of compensation capacitance C_p at the primary side, the voltage gain $G_v(j\omega)$ can be tuned to ensure that characteristics of input impedance become slightly inductive, hence satisfying soft-switching requirements.

Fig. 5 is the voltage gain depicted based on the parameters of Table I when the coil module is arranged as radial symmetry shown in Fig. 7. In the curve of Fig. 5, the solid line curve of G_v presents the frequency response when the duty cycle of each inverter is set at 35%, where the receiving coil is aligned with the transmitting one. This curve indicates the gain value at 86 kHz is 13.2 dB that stands for a resonant voltage gain of 4.57, which can be adjusted based on the output voltage and

delivered power. In addition, the dotted line curves of G_{as} (coil L_a), G_{bs} (coil L_b), and G_{cs} (coil L_c) are individually obtained at 40%, 35%, and 30% duty cycle of v_{ha}, v_{hb}, and v_{hc}, revealing that the relationships is consistently formed between the output power and voltage gain of each inverter. The voltage gain of $G_{as}(j\omega)$, $G_{bs}(j\omega)$, and $G_{cs}(j\omega)$ expressed for the voltage on the receiving coil to that on each transmitting coil of L_a, L_b, and L_c can be further expressed as

$$G_{ns}(j\omega) = \left|\frac{v_s(j\omega)}{v_{hn}(j\omega)}\right| = \left|\frac{3j\omega M_{tr}}{Z_{in-n}(j\omega)} \times \frac{\frac{R_L}{1+j\omega C_s R_L}}{j\omega L_s + \frac{R_L}{1+j\omega C_s R_L}}\right| \tag{9}$$

where n stands for a, b, or c. Through this analysis, the key finding of Fig. 5 lies in a better comprehension of the variation of voltage gain when the system is operated at the certain frequency, by which it benefits the determination of the duty cycles of v_{ha}, v_{hb}, and v_{hc}, thus grasping the amount of power and voltage (v_s) to be delivered in a more effective way. Meanwhile, based on the frequency ranging from 83 to 89 kHz shown in Fig. 5, it reveals that the system would come with a stable voltage output because of the smooth curve gained from the relations between operating frequency and voltage gain. This figure can serve as the reference for the duty cycle planning once there is any change of operating frequency.

III. Interoperable Coil Module Design

A. Determination of Coil Module

Considering coil geometry and overlapping areas may affect the magnetic flux at the transmitting side, this section first examines the placement of coil module. For this coil design, the ferrite magnetic material of high permeability is adopted to improve the magnetic coupling for AGV applications. Fig. 6 shows the simulation curves of coupling coefficient k when circular and square coils are individually used with a diameter of 400 mm and a 20% winding fullness. A misalignment of 80 mm at the direction of horizontal and axial movement is concerned here for the simulation since it is the maximum misalignment of receiving coil encountered in our AGV station. As depicted in the figure, although the circular coil is seen to demonstrate a larger coupling at fixed points, the square coil exhibits a higher tolerance of misalignment [30], [31].

Fig. 6 also shows the experiment made for the comparison of coupling coefficient k under three-to-one and one-to-one square coil with the same module diameter. In this figure, the three-to-one structure demonstrates a smaller decrement of coupling coefficient with a horizontal displacement, confirming that this coil module comes with a higher tolerance of misalignment. As shown in Fig. 6(b) and (c), the comparison is made between one-to-one and three-to-one module with the same outer diameter of transmitting pad (600 mm × 600 mm) and receiving pad (400 mm × 400 mm) when operated at misalignment of 80 mm condition. Simulation results reveal that the three-square-coil structure reaches a more uniform magnetic field and exhibits a better misalignment-insensitive capability, thereby supporting

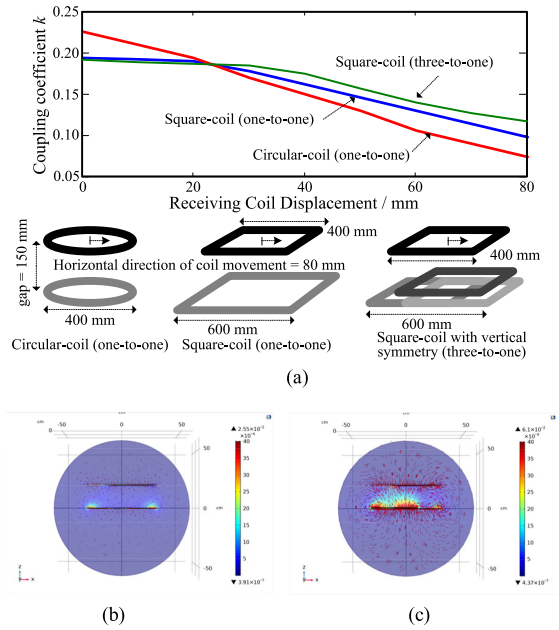

Fig. 6. (a) Coupling coefficient k of different geometric structures of coils and simulation results of magnetic field of (b) one-to-one square coil and (c) three-to-one square coil.

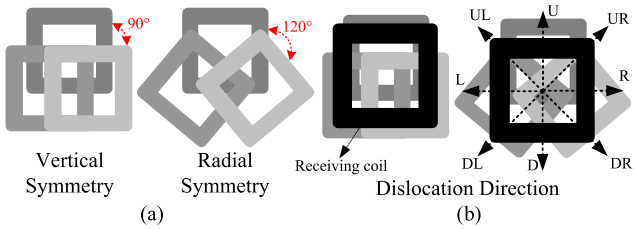

Fig. 7. (a) Geometric arrangements of three transmitting coils. (b) Different directions of movement of receiving coil.

the feasibility of the three-to-one coil module used in this article. Note that a transmitter structure composed of more than three coils was also evaluated in the article, yet its coil pad cost and complexity of coupling characteristics are significantly increased but with a limited improvement only [18]. Therefore, the configuration of the transmitter composed of three square coils is employed for this article.

Subsequently, the article evaluates the placement of three coils at the transmitting side. Fig. 7(a) depicts coil arrangements, including vertical symmetry and radial symmetry. Fig. 7(b) draws eight directions of receiving coil's movement. The movements of horizontal right and left (R and L), horizontal up and down (U and D), diagonal upper right and down left (UR and DL), and diagonal upper left and down right (UL and DR) are all concerned. For the horizontal misalignments, test results indicate that there is no significant difference among them. Yet, for the diagonal misalignment, Fig. 8 indicates that the radial symmetry presents a larger coupling coefficient, which consolidates the selection of radial symmetry for the coil arrangement in this article [24].

Fig. 9 shows the flowchart of design procedure of interoperable coil module. The procedure starts with the specification

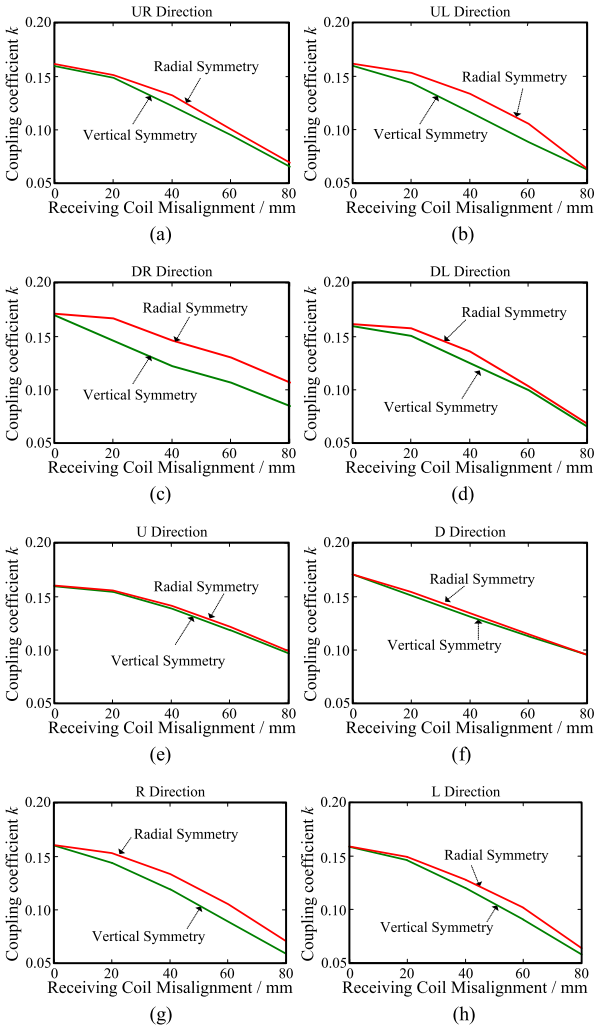

Fig. 8. Coupling coefficient of radial symmetry and vertical symmetry arrangement when misalignment happens under the horizontal movement of (a) up-right direction, (b) up-left direction, (c) down-right direction, and (d) down-left direction, (e) up direction, (f) down direction, (g) right direction, and (h) left direction.

of system parameters, transmission gap, dimension, and shape, where the coupling coefficient of 0.15 under the aligned condition is anticipated. In the article, the output power is selected to be 3.2 kW and the receiving coil has an air gap of 200 mm from the transmitting coils. Since the transmitting module allows a maximum diameter of 600 mm considering the space of charging roadway and lattices of IPT charging stations for AGV, each size of three transmitting coils is 400 mm × 400 mm (the inner diameter is 200 mm × 200 mm), while the size of single receiving coil is 500 mm × 500 mm (the inner diameter is 200 mm × 200 mm). As described in Fig. 9, only until the achievement of expected coupling efficient is confirmed, the coil winding can be made based on analysis results. The angle between the central axes of each transmitting coil is 120 degree. The sketch of coil placement is added in the flowchart of Fig. 9. These three transmitting coils can be moved inward or outward to adjust the overlapping area so as to satisfy the request of transmitting pad, hence reaching a higher coupling performance when operated at misalignment conditions.

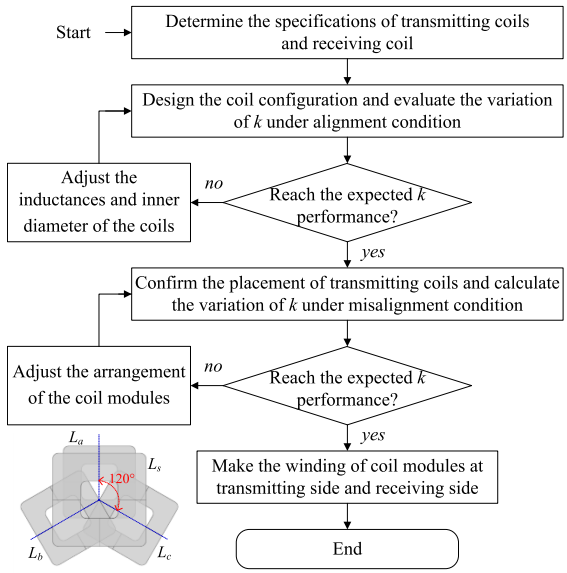

Fig. 9. Design procedure of coil module.

B. Realization of Inductive Coils

In this article, the Litz wire of 0.08 mm diameter with 500 strands of no. 40 AWG is adopted. The ferrite core with a high relative permeability of 1500 (the dimension is 600 mm × 600 mm × 3 mm) is incorporated at the top and bottom side of tricoil module such that a better coupling is attained. Three transmitting coils of L_a–L_c are individually measured to be 65.64 μH, 67.42 μH, and 66.34 μH, while the receiving coil of L_s is 44.76 μH. Measured results indicate that each M_{tr} and M_{tt} are approximately equal to 8.336 μH and 5.755 μH, respectively, and k_{tr} and k_{tt} are near 0.153 and 0.113, respectively. With the uniform arrangement of transmitting coils through the modular jig and fixture tool, the overlapping area between coils can be tuned to be similar to each other, which is in good agreement with theoretical derivations of Section II(B).

Fig. 10(a) and (b) shows the photograph of coil module consisting of three transmitting coils and one receiving coil. The coil winding is made via modular jig and fixture based on the radial symmetry arrangement, which excels at maintaining a certain level of efficiency whenever the mass production is concerned. Fig. 10 (c) and (d) shows the simulation results of magnetic field distribution of three transmitting coils and one receiving coil. In the plot of Fig. 10(c), the magnetic field around the coil is seen to be distributed uniformly, benefiting the coupling stability under the misalignment. Then, in Fig. 10(d), the leakage magnetic flux is relatively smaller than the coil coupling, supporting the low rotating coupling loss of the coil arrangement in this article. Table I lists the parameters of system. Following the calculation of compensation capacitance C_p and C_s to achieve the zero-voltage switching, the transmitting capacitances C_a, C_b, and C_c of 64.62 nF, 66.48 nF, and 65.62 nF are obtained.

C. Coupling Analysis of Coil Misalignment

The article next investigates the voltage gain under different coupling coefficients and various directions of misalignment.

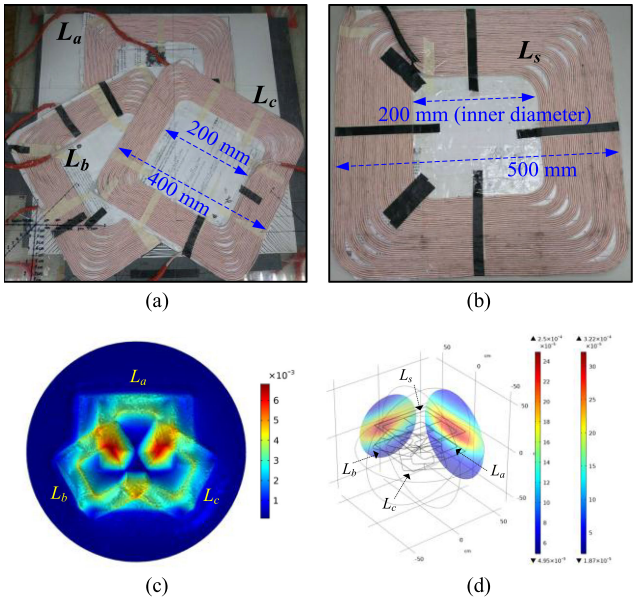

Fig. 10. (a) Placement of three transmitting coils. (b) Placement of one receiving coil. (c) Simulation results of magnetic field distribution. (d) Simulation results of magnetic flux leakage.

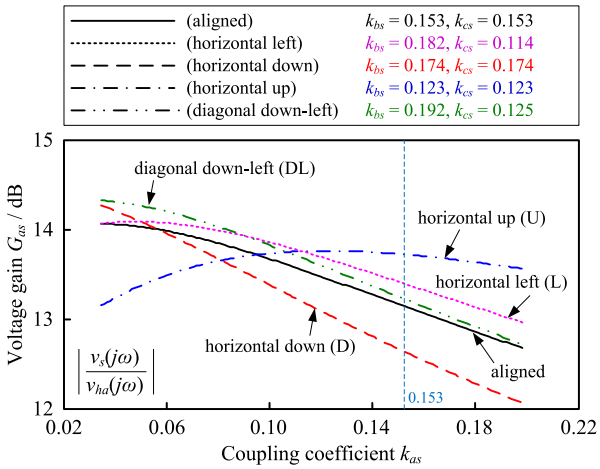

Fig. 11. Calculation results of voltage gain G_{as} as a function of coupling coefficient when the receiving coil L_s is misaligned with the transmitting coil.

Analysis results are helpful for the controller to adjust the output power of each inverter. The test setup begins with the system parameter and geometrical of tricoil module of Table I and Fig. 10. The analysis goes with the coil L_a for the calculation of voltage gain G_{as}, through which the test procedure is applicable to L_b and L_c such that the voltage gain G_{bs} and G_{cs} can be accordingly obtained. The test setup procedure includes the following: 1) the receiving coil L_s is aligned; 2) the receiving coil L_s is misaligned; and 3) the receiving coil L_s is misaligned along with the variation of coupling characteristics. Fig. 11 shows the voltage gain of G_{as} obtained under misalignment conditions, where k_{as}, k_{bs}, and k_{cs} are coupling coefficients between coils L_a–L_c and L_s, respectively. Considering that the coupling between L_a and L_s is possibly affected by foreign object intrusion or fractured coil, the variation of k_{as} is served as

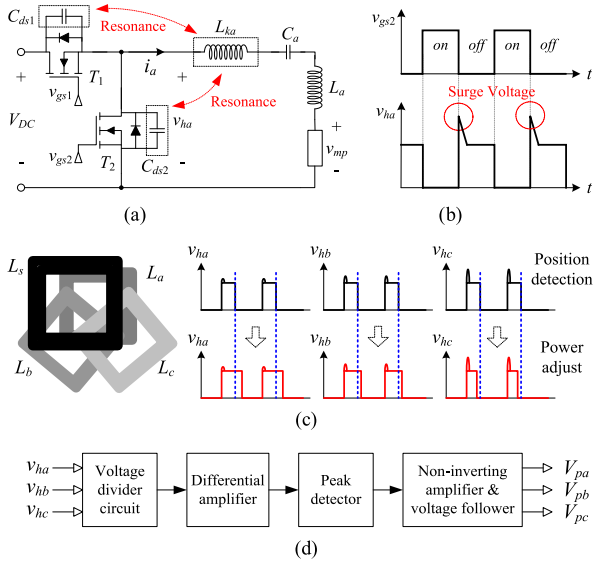

Fig. 12. Misalignment detection technique. (a) Resonance between leakage inductance and parasitic capacitances. (b) Peak voltage of power switch T_2. (c) Voltage-peak detection under the scenario of misalignment. (d) Function block of voltage detection circuit.

the x-axis to investigate the gain variation of G_{as}. In this figure, the solid line is drawn when the receiving coil L_s is aligned with the transmitting coil. At this time, the figure indicates that the G_{as} is about 13.2 dB when the coupling coefficient of k_{tr} is equal to 0.153, as observed from Fig. 5. Yet, when the coil L_s moves to the horizontal left (L), horizontal down (D), or diagonal down right (DL), the dashed line indicates that the coupling coefficient of k_{as} is reduced following the increased gain of G_{as}. When encountered such a misalignment, the output power and voltage v_{ha} of inverter would decrease. On the contrary, when the coil L_s moves at the direction of horizontal up (U), the dashed line shows that the coupling coefficient of k_{as} increases following the decrement of G_{as}, in which the output power and voltage v_{ha} of inverter would increase. In other words, through the flexible power control based on the variation of coupling coefficient (k_{as}, k_{bs}, and k_{cs}) with respect to voltage gain (G_{as}, G_{bs}, and G_{cs}), the misalignment-insensitive capability of IPT is presented.

IV. Dynamic Power Control Mechanism

It is crucial to ensure that the efficiency of power transmission is less affected once misalignment happens. In this section, the misalignment detection of receiving coil is examined [32]. Both misalignment detection method and automatic power adjustment are discussed.

A. Misalignment Detection Technique

To early detect the misalignment, this article proposes a voltage-peak-based method to help grasp the moving direction of receiving coil. As Fig. 12(a) depicts, a circuit loop used for the release of stored energy may cause the resonance occurred either between leakage inductance L_{ka} and parasitic capacitance

C_{ds1}–C_{ds2} or on the layout path of parasitic capacitances and parasitic inductances, resulting in a voltage spike when the switch T_2 is turned off, as shown in Fig. 12(b). It is also worth observing that the voltage v_{ha} of switch T_2 in Fig. 12(a) is not only affected by the leakage inductance and parasitic components, but also influenced by the mutual inductance-coupled voltage of v_{mp} that is mapped from the secondary to the primary side. The voltages equations of v_{ha} and v_{mp} are expressed as

$$v_{ha} = \left(\frac{1}{j\omega C_a} + j\omega L_a + j\omega L_{ka}\right) i_a + v_{mp} \tag{10}$$

$$v_{mp} = \frac{\omega^2 M_{tr}^2 (i_a + i_b + i_c)}{j\omega L_s + \frac{R_L}{1+j\omega C_s R_L}} + j\omega M_{tt}(i_b + i_c). \tag{11}$$

Equation (11) reveals that voltage v_{mp} varies after the change of mutual inductance $M_{tr.}$ as well as the effect of secondary coil inductance L_s and capacitance C_s. Following the high-frequency variation of inductor current of di_a/dt during the switching of T_2, the coil inductance L_{coil}, the parasitic inductance $L_{\text{parasitic}}$, and the leakage inductance L_{ka} cooperatively induce a surge voltage ringing across the drain and the source of switch T_2. Then, as expressed in (10), the peak amplitude and surge voltage of v_{ha} are meanwhile affected by the resonance of leakage inductance, parasitic components, and the change of misalignment. This surge voltage is expressed as

$$v_{ha(\text{surge})} = (L_{\text{coil}} + L_{\text{parasitic}} + L_{ka})\frac{di_a}{dt} \tag{12}$$

where L_{coil}, $L_{\text{parasitic}}$, and L_{ka} are coil inductance, parasitic inductance, and leakage inductance, respectively. Therefore, the corresponding variation of voltage peak becomes beneficial for serving as an indicator to alert the occurrence of misalignment. For example, as Fig. 12(c) depicts, when the receiving coil L_s is not aligned and the distance between L_s and L_a is the shortest one, then the peak amplitude of v_{ha}, v_{hb}, and v_{hc} indicate that v_{ha} is the smallest one. At this time, the receiving coil is justified near L_a, and the duty cycle of corresponding switch can be accordingly adjusted [31]–[34], thereby completing the task of misalignment detection in this article. Fig. 12(d) shows that the function block of voltage detection circuit, the high-impedance voltage divider and differential amplifier are designed to tune the voltage ratio, by which the peak-value sampling circuit is employed to acquire the maximum voltage and feed into the controller. This way of circuit design saves the cost of voltage sensors, while the signal distortion caused by magnetic elements operated at the high frequency range is avoided.

B. Controllable Power Output

Fig. 13 shows the design of dynamic power control. The system starts with the voltage detection circuit to obtain the voltage v_h across each power switch at the transmitting side. This is followed by the signal V_p of voltage peak delivered to the microcontroller to determine if the receiving coil is misaligned. In other words, based on the output dc voltage of V_{pa}, V_{pb}, and V_{pc} , as shown in Fig. 12(d), they are employed as the reference to detect the location of receiving coil and adjust the power

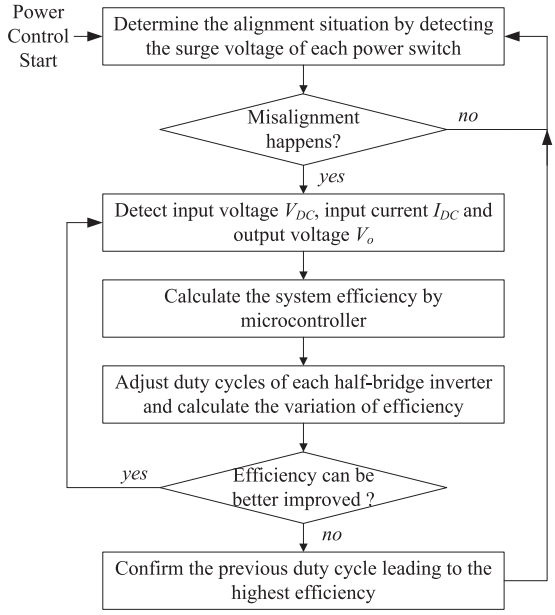

Fig. 13. Flowchart of dynamic power control.

dynamically. Once any misalignment happens, the data of input voltage (V_{dc}), input current (I_{dc}), and output voltage (V_o) are sent to a microcontroller via a data acquisition circuit so that the system efficiency can be immediately calculated. For example, when L_s moves near L_a and away from L_c , as delineated in Fig. 12(c), the voltage V_{pc} becomes higher than V_{pa} and V_{pb}, and the V_{pa} is lower than V_{pb} and V_{pc}, indicating that the misalignment happens. At this time, the controller immediately sends the command to decrease the duty cycle of v_{hc} and increase the duty cycle of v_{ha} such that the magnetic field density of receiving coil will be enhanced. Subsequently, the efficiency is calculated again. Only when the efficiency is no further improved, then the system confirms that duty cycle of each inverter is well adjusted, hence reaching the goal of dynamic power control [31]–[36]. In other words, with the selective energization of a certain coil depending on the way of coil movement, the merits of the proposed method include the following: 1) a higher efficiency of charging under the misalignment; 2) a more effective way of reducing the flux leakage; and 3) a systematic approach of coping with multicoil IPT.

V. Experimental Results

To validate the misalignment-insensitive capability of the proposed method, the article realizes a hardware circuit system as photographed in Fig. 14, including three half-bridge resonant inverters, compensation capacitors, wireless power transfer platform, full-wave rectifier, and filter circuit. It is also noted that a ferrite pad is incorporated at the top side of receiving coil and bottom side of coil module, achieving a better coupling.

A. Tricoil Module and IPT Circuit Test

In this test, the receiving coil is situated straight above the transmitting coil module. Being operated at the frequency of

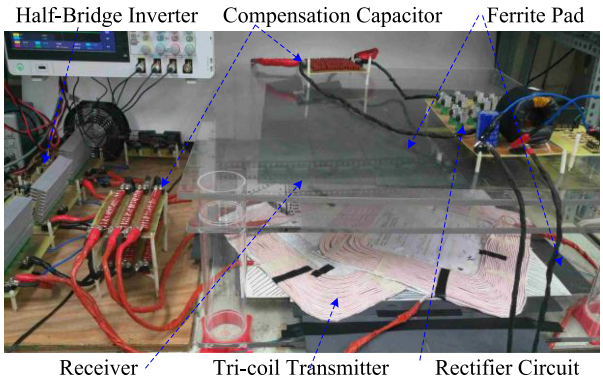

Fig. 14. Photograph of hardware circuit realization.

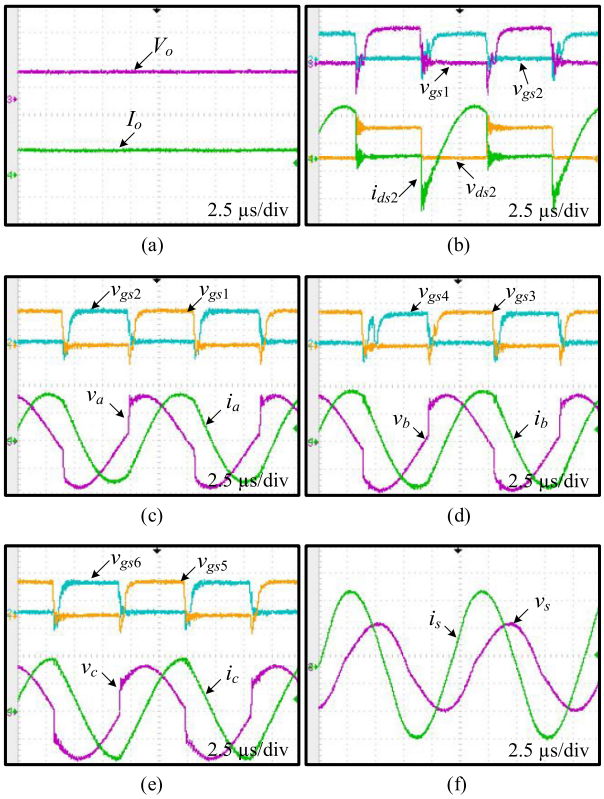

Fig. 15. Experimental waveforms operated at 200 mm air gap under full load condition. (a) Output voltage V_o and output current I_o. (b) Waveforms of one half-bridge inverter including v_{gs1},v_{gs2},v_{ds2}, and i_{ds2}. (c) Switching signals of V_{gs1} and V_{gs2}, and waveforms of transmitting coil L_a including v_{La} and i_{La}. (d) Switching signals of V_{gs3} and V_{gs4}, and waveforms of transmitting coil L_b including v_{Lb} and i_{Lb}. (e) Switching signals of V_{gs5} and V_{gs6}, and waveforms of transmitting coil L_c including v_{Lc} and i_{Lc}. (f) Waveforms of receiving coil L_s including v_s and i_s (V_o: 400 V/div, I_o: 10 A/div, v_{gs1}–v_{gs6}: 10 V/div, v_{ds2}: 400 V/div, i_{ds2}: 10 A/div, i_a–i_c: 10 A/div, v_a–v_c: 400 V/div, i_s: 10 A/div, and v_s: 400 V/div).

86 kHz and 200 mm air gap along with dc input voltage $V_{\rm dc}$ of 415.6 V, this system reaches the output power P_o of 3.2 kW with stable output voltage and transmission efficiency of 87.5% when connected with the equivalent dummy load R_V of 48 Ω. As shown in Fig. 15(a), the output voltage V_o and output current I_o at the load side are 393.9 V and 8.21 A, respectively, indicating that the output power capability is 3.2 kW. Fig. 15(b) shows the soft-switching test of half-bridge inverter under a full-load condition.

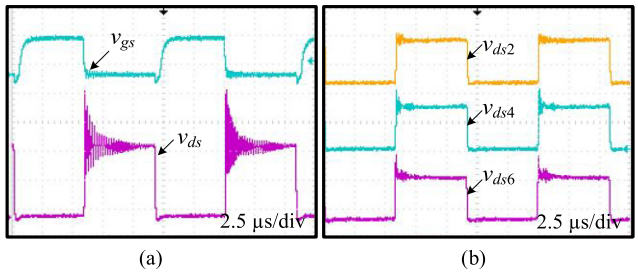

Fig. 16. Experimental waveforms of misalignment detection. (a) Switching signal v_{gs} and voltage v_{ds} of the power switch in the half-bridge inverter. (b) Three surge voltages v_{ds2},v_{ds4}, and v_{ds6} are measured at different inverters under 100 mm misalignment (v_{gs}: 10 V/div, v_{ds}: 200 V/div, v_{ds2}–v_{ds6}: 200 V/div).

In this figure, two switching signals v_{gs1} and v_{gs2} of one half-bridge inverter as well as v_{ds2} and i_{ds2} of one single switch are depcited. Experimental waveforms show that the zero-voltage switching of power switches is achieved.

Fig. 15 (c)–(e) delineates voltage waveforms of v_a, v_b, and v_c, and current waveforms of i_a, i_b, and i_c of three transmitting coils. These waveforms demonstrate that the voltage and current of each tranmitting coil are simular to each other. The delivered power is proved to be balanced and the magnetic field can be evenly distributed for each coil. Subsequently, in Fig. 15(f), v_s and i_s of receiving coil validate that the wireless power is transmitted to the load side, confirming the practicality of the method.

B. Coil Misalignment Test

This section inspects the variation of voltage v_{ds} across the power switch when the receiving coil is misaligned. In this experiment prototype, we have predetermined a maximum tolerance value of 900 V for the detection task. We have also measured the maximum surge voltage of 750–800 V when the misalignment is about 250 mm that is larger than a transmitting coil. It was found that the sufficient margin is reserved for the coil misalignment. Fig. 16(a) shows the switching signal v_{gs} and the voltage v_{ds} across one power switch when the system is operated at 3 kW output power. A surge voltage rining is seen to exist in waveforms that may be caused by resonance between leakage inductance L_k of the circuit path and parasitic capacitance C_{ds} of the power switch, or the mutual inductance-coupled voltage v_{mp} mapped from the receiving side to the transmitting side. The test is made with a horizontal displacement of 100 mm of the receiving coil related to the transmitting coil L_a. Fig. 16(b) shows the voltages v_{ds2}, v_{ds4}, and v_{ds6} across the power switch of each half-bridge inverter. At this time, the peak voltage of v_{ds2} reaches 344 V when the surge peak of v_{ds4} and v_{ds6} reaches 424 V and 448 V, respectively, indicating that the peak voltage of tranmitting coil L_a is much lower than that of others. This situation happens because the coupling coefficient between receiving coil and coil L_a increases once the receiving coil moves towards L_a. Accordingly, once the direction of coil movement is identified, a dynamic power control is employed. Note that the dc voltage $V_{\rm dc}$ of 300 V is adopted in Fig. 16(b), which is

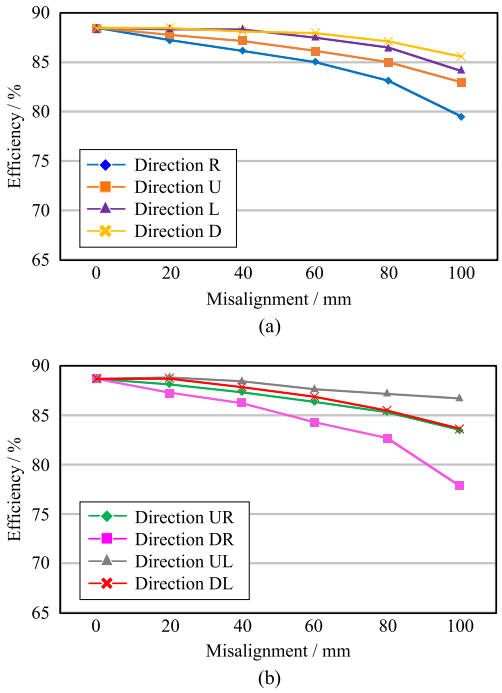

Fig. 17. Efficiency measurements in eight directions of coil misalignment. (a) Misalignment of receiving coil in the direction of right (R), up (U), left (L), and down (D). (b) Misalignment of receiving coil in the direction of up-right (UR), down-right (DR), up-left (UL), and down-left (DL).

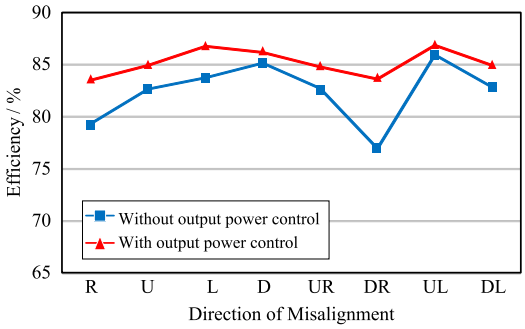

Fig. 18. Efficiency measurements under a 100-mm misalignment with and without dynamic control in eight directions of movement.

aimed to validate the detection capability of the circuit under the scenario of peak voltage variations.

Fig. 17 shows the efficiency meaurement of eight misaligned directions without dynamic power control when the system is operated at 3.2-kW output power. In the figure, for all directions of receiving coil's movement at the misalignment of 100 mm, an efficiency of 81.8%–87.5% can be obtained. It is observed that even if the coil L_c is placed on the top of three coils and the symmetrical placement is not fully acheived, the efficiency is only slightly affected. With the proposed three transmitting coil structures, the figure confirms that only a 6.5% efficiency decrement is measured at the misalignment of 100 mm.

Based on the test condition and results of Fig. 17, Fig. 18 shows the system efficiency of the proposed interoperable coil module consisting of three transmitting coils and one receiving coil. This test is made with and without dynamic power control at 100 mm misalignment of receiving coil in eight directions. Experimental outcome shows that the efficiency of IPT becomes higher than 83.5% via dynamic power control in all eight directions of coil movement.

VI. Conclusion

The article proposes an interoperable coil module-based misalignment-insensitive IPT with the capability of dynamic power control. With the analysis of magnetic field distribution of coil configuration and arrangement, an inductive power transmission structure is completed with radial placement of three coils. The article includes misalignment detection method and dynamic power control technique to adjust power switches of inverters with tests carried out under different scenarios. The coupling condition of the module is tested satisfactory under different directions of coil misalignment. The outcomes support the feasibility of the proposed circuit design, facilitating the realizainig of this approach applied for AGV-charging applications.

References

[1] J. M. Miller, O. C. Onar, and M. Chinthavali, "Primary-side power flow control of wireless power transfer for electric vehicle charging," *IEEE J. Emerg. Sel. Topics Power Electron.*, vol. 3, no. 1, pp. 147–162, Mar. 2015.
[2] S. G. Liu, Y. Guo, H. Li, and G. Cai, "Double-LCL resonant compensation network for electric vehicles wireless power transfer: Experimental study and analysis," *IET Power Electron.*, vol. 9, no. 11, pp. 2262–2270, Sep. 2016.
[3] J. Gozalvez, "First wireless electric vehicle charging trial," *IEEE Veh. Technol. Mag.*, vol. 7, no. 2, pp. 10–17, Jun. 2012.
[4] F. Musavi and W. Eberle, "Overview of wireless power transfer technologies for electric vehicle battery charging," *IET Power Electron.*, vol. 7, no. 1, pp. 60–66, Jan. 2014.
[5] Y. C. Hsieh, Z. R. Lin, M. C. Chen, H. C. Hsieh, Y. C. Liu, and H. J. Chiu, "High-efficiency wireless power transfer system for electric vehicle applications," *IEEE Trans. Circuits Syst. II, Exp. Briefs*, vol. 64 no. 8, pp. 942–946, Nov. 2016.
[6] J. M. Miller and A. Daga, "Elements of wireless power transfer essential to high power charging of heavy duty vehicles," *IEEE Trans. Transp. Electrific.*, vol. 1, no. 1, pp. 26–39, Jun. 2015.
[7] M. Kim, H. Kim, D. Kim, Y. Jeong, H. H. Park, and S. Ahn, "A three-phase wireless-power-transfer system for online electric vehicles with reduction of leakage magnetic fields," *IEEE Trans. Microw. Theory Techn.*, vol. 63, no. 11, pp. 3806–3813, Nov. 2015.
[8] J. Schneider, "SAE TIR J2954 wireless charging of electric and plug-in hybrid vehicles," *SAE Int*.
[9] S. H. Lee, B. S. Lee, and J. H. Lee, "A new design methodology for a 300-kW, low flux density, large air gap, online wireless power transfer system," *IEEE Trans. Ind. Appl.*, vol. 52, no. 5, pp. 4234–4242, Sep./Oct. 2016.
[10] J. Wang *et al.*, "Study and experimental verification of a rectangular printed-circuit board wireless transfer system for low power devices," *IEEE Trans. Magn.*, vol. 48, no. 11, pp. 3013–3016, Nov. 2012.
[11] T. C. Beh, M. Kato, T. Imura, S. Oh, and Y. Hori, "Automated impedance matching system for robust wireless power transfer via magnetic resonance coupling," *IEEE Trans. Ind. Electron.*, vol. 60, no. 9, pp. 3689–3698, Sep. 2013.
[12] Y. Lim and J. Park, "A novel phase-control-based energy beamforming techniques in nonradiative wireless power transfer," *IEEE Trans. Power Electron.*, vol. 30, no. 11, pp. 6274–6287, Nov. 2015.
[13] J. Zhou, B. Luo, X. Zhang, and Y. Hu, "Extendible load-isolation wireless charging platform for multi-receiver applications," *IET Power Electron.*, vol. 10, no. 1, pp. 134–142, Jan. 2017.
[14] Y. Zhang, T. Lu, Z. Zhao, F. He, K. Chen, and L. Yuan, "Employing load coils for multiple loads of resonant wireless power transfer," *IEEE Trans. Power Electron.*, vol. 30, no. 11, pp. 6174–6181, Nov. 2015.
[15] Y. Zhang, T. Lu, Z. Zhao, K. Chen, F. He, and L. Yuan, "Wireless power transfer to multiple loads over various distances using relay resonators," *IEEE Microw. Compon. Lett.*, vol. 25, no. 5, pp. 337–339, May 2015.

[16] M. Fu, T. Zhang, C. Ma, and X. Zhu, "Efficiency and optimal loads analysis for multiple-receiver wireless power transfer systems," *IEEE Trans. Microw. Theory Techn.*, vol. 63, no. 3, pp. 801–812, Mar. 2015.
[17] J. J. Casanova, Z. N. Low, and J. Lin, "A loosely coupled planar wireless power system for multiple receivers," *IEEE Trans. Ind. Electron.*, vol. 56, no. 8, pp. 3060–3068, Aug. 2009.
[18] S. Kim, G. A. Covic, and J. T. Boys, "Tripolar pad for inductive power transfer systems for EV charging," *IEEE Trans. Power Electron.*, vol. 32, no. 7, pp. 5045–5057, Jul. 2017.
[19] K. Lee and D. H. Cho, "Diversity analysis of multiple transmitters in wireless power transfer system," *IEEE Trans. Magn.*, vol. 49, no. 6, pp. 2946–2952, Jun. 2013.
[20] R. Johari, J. V. Krogmeier, and D. J. Love, "Analysis and practical considerations in implementing multiple transmitters for wireless power transfer via coupled magnetic resonance," *IEEE Trans. Ind. Electron.*, vol. 61, no. 4, pp. 1774–1783, Apr. 2014.
[21] H. D. Lang, A. Ludwig, and C. D. Sarris, "Convex optimization of wireless power transfer systems with multiple transmitters," *IEEE Trans. Antennas Propag.*, vol. 62, no. 9, pp. 4623–4636, Sep. 2014.
[22] I. J. Yoon and H. Ling, "Investigation of near-field wireless power transfer under multiple transmitters," *IEEE Antennas Wireless Propag. Lett.*, vol. 10, pp. 662–665, June 2011.
[23] S. Y. R. Hui and W. W. C. Ho, "A new generation of universal contactless battery charging platform for portable consumer electronic equipment," *IEEE Trans. Power Electron.*, vol. 20, no. 3, pp. 620–627, May 2005.
[24] S. Kim, G. A. Covic, and J. T. Boys, "Comparison of tripolar and circular pads for IPT charging systems," *IEEE Trans. Power Electron.*, vol. 33, no. 7, pp. 6093–6103, Jul. 2018.
[25] B. C. Kim, K. B. Park, and G. W. Moon, "Asymmetric PWM control scheme during hold-up time for LLC resonant converter," *IEEE Trans. Ind. Electron.*, vol. 59, no. 7, pp. 2992–2997, Jul. 2012.
[26] T. S. Lee, S. J. Huang, R. Y. Chen, and Y. H. Yeh, "Enhancement of plasma-driven system with piezoelectric transformer-based feedback control approaches and contactless power source," *IEEE Trans. Ind. Electron.*, vol. 62, no. 12, pp. 7469–7478, Dec. 2015.
[27] W. Zhong and S. Y. R. Hui, "Maximum energy efficiency operation of series-series resonant wireless power transfer systems using on-off keying modulation," *IEEE Trans. Power Electron.*, vol. 33, no. 4, pp. 3595–3603, May 2017.
[28] C. S. Wang, G. A. Covic, and O. H. Stielau, "Power transfer capability and bifurcation phenomena of loosely coupled inductive power transfer system," *IEEE Trans. Ind. Electron.*, vol. 51, no. 1, pp. 148–157, Feb. 2004.
[29] Z. N. Low, R. A. Chinga, R. Tseng, and J. Lin, "Design and test of a high-power high-efficiency loosely coupled planar wireless power transfer system," *IEEE Trans. Ind. Electron.*, vol. 56, no. 5, pp. 1801–1812, May 2009.
[30] F. Y. Lin, S. Kim, G. A. Covic, and J. T. Boys, "Effective coupling factors for series and parallel tuned secondaries in IPT system using bipolar primary pads," *IEEE Trans. Transport. Electrific.*, vol. 3, no. 2, pp. 434–444, Jun. 2017.
[31] G. R. Nagendra, G. A. Covic, and J. T. Boys, "Sizing of inductive power pads for dynamic charging of EVs on IPT highways," *IEEE Trans. Transport. Electrific.*, vol. 3, no. 2, pp. 405–417, Jun. 2017.
[32] S. Y. Jeong, V. X. Thai, J. H. Park, and C. T. Rim, "Self-inductance-based metal object detection with mistuned resonant circuits and nullifying induced voltage for wireless EV chargers," *IEEE Trans. Power Electron.*, vol. 34, no. 1, pp. 748–758, Jan. 2019.
[33] L. Zhao, D. J. Thrimawithana, U. K. Madawala, P. Hu, and C. C. Mi, "A misalignment tolerant series-hybrid wireless EV charging system with integrated magnetics," *IEEE Trans. Power Electron.*, vol. 34, no. 2, pp. 1276–1285, Feb. 2019.
[34] L. Zhao, D. J. Thrimawithana, and U. K. Madawala, "Hybrid bidirectional wireless EV charging system tolerant to pad misalignment," *IEEE Trans. Ind. Electron.*, vol. 64, no. 9, pp. 7079–7086, Sep. 2017.
[35] Y. Tang, Y. Chen, U. K. Madawala, D. J. Thrimawithana, and H. Ma, "A new controller for bidirectional wireless power transfer systems," *IEEE Trans. Power Electron.*, vol. 33, no. 10, pp. 9076–9087, Oct. 2018.
[36] S. Y. Jeong, J. H. Park, G. P. Hong, and C. T. Rim, "Autotuning control system by variation of self-inductance for dynamic wireless EV charging with small air gap," *IEEE Trans. Power Electron.*, vol. 34, no. 6, pp. 5165–5174, Jun. 2019.

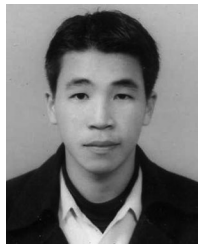

Tsong-Shing Lee received the Ph.D. degree in electrical engineering from National Cheng Kung University, Tainan, Taiwan, in 2015.

From 2004 to 2016, he was with AU Optronics Corporation, HsinChu, Taiwan. Since 2016, he has been with the Department of Electrical Engineering, Southern Taiwan University of Science and Technology, Tainan, Taiwan, where he is currently an Associate Professor. His research interests include power electronic converters, inductively coupled power transfer systems, display power supply, resonant circuit, and piezoelectric transformer power applications.

Shyh-Jier Huang (Senior Member, IEEE) received the Ph.D. degree in electrical engineering from the University of Washington, Seattle, WA, USA, in 1994.

He is a Distinguished Professor with the Department of Electrical Engineering, National Cheng Kung University, Tainan, Taiwan. His research interests include industrial electronics, power system, power electronics, and signal-processing applications.

Dr. Huang was a recipient of the Outstanding Research Award from the Ministry of Science and Technology of Taiwan in 2004, and the Outstanding Technical Achievement Award from IEEE Tainan Section in 2016. He was the IEEE Taipei Chapter Chair of the IEEE Power Engineering Society in 2002.

Shuo-Huei Dai was born in Chiayi, Taiwan, in 1995. He received the M.S. degree in electrical engineering from National Cheng Kung University, Tainan, Taiwan, in 2018.

He is currently with Himax Technologies, Inc., Tainan, Taiwan. His research mainly focuses on power electronics, especially the application of wireless charging for consumer and industrial purposes.

Jun-Li Su was born in Tainan, Taiwan, in 1995. He received the B.S. and M.S. degrees from National Cheng Kung University, Tainan, Taiwan, in 2017 and 2018, respectively, both in electrical engineering.

He was with MediaTek, Inc., Hsinchu, Taiwan, from 2018 to 2019, and is currently with Delta Electronics, Inc., Tainan, Taiwan. His research interests include power electronics, wireless power transfer, and firmware system for power supply development.